AGU PUBLICATIONS

JGR

Journal of Geophysical Research: Oceans

RESEARCH ARTICLE

10.1002/2013JC009436

Energy dissipation in viscous-plastic sea-ice models

Amélie Bouchat[1] and Bruno Tremblay[1]

[1]Department of Atmospheric and Oceanic Sciences, McGill University, Montréal, Quebec, Canada

Key Point:
- Energy dissipated in the nonphysical viscous deformations is negligible

Correspondence to:
A. Bouchat,
amelie.bouchat@mail.mcgill.ca

Citation:
Bouchat, A., and B. Tremblay (2014), Energy dissipation in viscous-plastic sea-ice models, *J. Geophys. Res. Oceans*, *119*, 976–994, doi:10.1002/2013JC009436.

Received 13 SEP 2013
Accepted 14 JAN 2014
Accepted article online 22 JAN 2014
Published online 12 FEB 2014

Abstract In viscous-plastic (VP) sea-ice models, small deformations are approximated by irreversible viscous deformations, introducing a nonphysical energy sink. As the spatial resolution and the degree of numerical convergence of the models increase, linear kinematic features (LKFs) are better resolved and more states of stress lie in the viscous regime. Energy dissipation in this nonphysical viscous regime therefore increases. We derive a complete kinetic energy (KE) balance for sea ice, including plastic and viscous energy sinks to study energy dissipation. The main KE balance is between the energy input by the wind and the dissipation by the water drag and the internal stresses (dissipating 87% and 13% of the energy input on an annual average). The internal stress term is mostly important in winter when ice-ice interactions are dominant. The energy input that is not dissipated locally is redistributed laterally by the internal stresses into regions of dissipation by small-scale deformations (LKFs). Of the 13% dissipated annually by the internal stress term, 93% is dissipated in plastic friction along LKFs (14% in ridging, 79% in shearing) and 7% is stored as potential energy in ridges. For all time and spatial scales tested, the frictional viscous dissipation is negligible in the KE balance. This conclusion remains valid regardless of the degree of numerical convergence of the simulations. Overall, the results confirm the applicability, from an energetical point of view, of the VP approximation.

1. Introduction

Satellite images from the RADARSAT Geophysical Processor System (RGPS) show that Arctic sea-ice deformations occur mostly along narrow lines of high strain rates (called Linear Kinematic Features—LKFs), while the surrounding pack undergoes no or very small deformations [*Kwok*, 2001]. These deformations are simulated via a constitutive equation (or rheology) that relates the sea-ice deformations (or strain rates) to the internal stresses. Early models of sea ice considered ice as a viscous material [*Campbell*, 1965; *Glen*, 1970], but these were soon abandoned for plastic models based on the observation that the work done in deforming the ice is independent of the deformation rate [*Coon et al*., 1974]. As part of the Arctic Ice Dynamics Joint EXperiment (AIDJEX), *Coon et al*. [1974] developed an elastic-plastic (EP) rheology in which large plastic deformations would occur only after the internal stresses had reached a critical threshold (yield curve). In order to close the set of equations, they proposed an elastic response for subcritical stresses. In EP models, the energy input in the pack from the surface wind stress was dissipated by the water drag and plastic deformations only. Since elastic deformations are reversible, the work done by the wind is fully recovered when the stress is removed, i.e., there is no energy loss from this mechanism. Resolving reversible elastic deformation is numerically demanding because it requires small time steps and a record of the strain rate history. As a result, early EP models mainly focused on short-term simulations. Recent advances in numerical methods now allow EP models to run on longer time scales [*Pritchard*, 2001].

As a simplification to the EP model, *Hibler* [1977] developed a viscous-plastic (VP) rheology combining both the early viscous theories and the plastic behavior presented by *Coon et al*.'s [1974] model. *Hibler* [1977] showed that the average of stochastic variations in small plastic deformations can be approximated by a viscous-like stress-strain relation. To this end, he proposed to approximate small deformations by the slow creep of a highly viscous fluid, while large deformations are still modeled as plastic. This assumption resulted in a considerable gain in numerical efficiency compared to the previous EP formulation and established the VP models as the standard sea-ice rheology. The new development of efficient numerical methods [*Zhang and Hibler*, 1997; *Hunke and Dukowicz*, 1997; *Lemieux et al*., 2008, 2010] now allows the VP model to be solved at increasingly high spatial resolution and on longer time scales.

In the VP model, a nonphysical energy sink is introduced since viscous deformations are irreversible. *Hibler* [1979] assumed that this energy dissipation would not affect the computations as long as the value of the strain rates delimiting the viscous and plastic deformations was chosen small enough. We raise the following questions: how large is the energy dissipated by viscous deformations? And, is it still negligible in VP models in the context of models being run at increasingly high spatial resolution and with increased numerical convergence?

In a study of the impacts of the spatial resolution and rheological model on the simulation of the LKFs with a VP model, *Wang and Wang* [2009] showed that the number of deformations lines increases with an increasing spatial resolution (from 10 to 2 km grids). Previous broad LKFs now appear as distinct finer LKFs. The refinement of the deformation lines implies that grid points previously part of the LKFs now undergo viscous deformations. We therefore expect an increase in the dissipation of energy in the nonphysical viscous regime as spatial resolution increase. Moreover, *Lemieux and Tremblay* [2009] showed the importance of calculating a converged solution to appropriately resolve LKFs. Better resolved LKFs again lead to more state of stress in the pack ice in the viscous (elastic) regime and less (albeit more active) state of stress in the plastic regime (see for instance *Zhang and Rothrock* [2000]). This, together with the fact that models are run at increasingly high spatial resolution, makes us question the validity of the VP approximation in current sea-ice models.

Energy equations are useful for characterizing sea-ice simulations because of their simple scalar interpretation. Early considerations on energy dissipation based on the principle that the work done in plastic deformation should be equal to the known energy sinks [*Parmerter and Coon*, 1973] have already been used in EP models to determine the temporal evolution of the ice strength in compression. The energy sinks considered at the time were parameterized as functions of the ice thickness distribution and included the potential energy change from the ridging process [*Coon et al*., 1974; *Thorndike et al*., 1975] and the frictional losses in ridging and shearing deformations [*Rothrock*, 1975; *Pritchard*, 1981]. An equation for the kinetic energy (KE) balance of sea ice was first developed within the EP formulation by *Coon and Pritchard* [1979]. Their application of the KE equation to a 1-D idealized example representing winter conditions in the Beaufort Sea shed light on the role of the internal stresses in the lateral transmission of energy via a stress flux term. *Pritchard* [1981] also studied the KE balance with the AIDJEX's EP model for sea ice in winter in the Beaufort Sea. Although he developed parametrizations for the energy sinks in potential energy and in frictional losses in ridging and shearing deformations, he did not include it in its temporal and spatial analysis of the KE balance. These three energy sinks were later quantified numerically for the first time in the VP model by *Steele et al*. [1997], who presented a (domain averaged) seasonal cycle of each term in the KE balance on a 40 km grid. To the best of our knowledge, no analysis including an energy sink for the rate of energy dissipation by viscous creep has been made for the VP model or a detailed quantification of each term in the local KE balance along with a study of the mechanisms of energy dissipation by the ice interaction term.

In this paper, we study the energy dissipation in VP models by computing a complete KE balance for sea ice, including an energy sink for the viscous dissipation. This allows us to quantify each term in the KE balance and to understand the mechanisms of redistribution and dissipation of the KE in the pack. The importance of the nonphysical dissipation in high resolution and converged simulations is also assessed to test the viscous approximation (with respect to energetics). We address these questions by presenting Arctic-mean and spatially varying seasonal cycles of each term in the KE balance using both monthly averaged and instantaneous fields, with a special attention to the redistribution and quantification of energy at different scales.

The paper is structured as follows. In sections 2 and 3, we present the momentum and continuity equations for sea ice and the specific equations for a viscous-plastic rheology. In section 4, we derive the KE balance including the energy sink for the viscous dissipation. In section 6, we discuss the results for the KE balance and its dependence on the grid resolution and the degree of convergence of the numerical solver. The main conclusions drawn from this study are presented in section 7.

2. Sea-Ice Momentum and Continuity Equations

The two-dimensional horizontal momentum equation for sea ice is given by:

$$\rho_i h\left[\frac{\partial \mathbf{u}}{\partial t}+(\mathbf{u}\cdot\nabla)\mathbf{u}\right]=-\rho_i h f\mathbf{k}\times\mathbf{u}+\tau_\mathbf{a}-\tau_\mathbf{w}+\nabla\cdot\boldsymbol{\sigma}-\rho_i h g\nabla H_d \ , \tag{1}$$

where ρ_i is the ice density, h the mean ice thickness, f the Coriolis parameter, $\mathbf{k}$ the vertical unit vector, $\mathbf{u}=(u,v)$ the horizontal sea-ice velocity, τ_a the surface wind stress, τ_w the water drag, σ the two-dimensional vertically integrated internal ice stress tensor, g is the gravitational acceleration, and H_d the sea surface height. The gravitational term can also be approximated as $-\rho_i h g\nabla H_d=\rho_i h f\mathbf{k}\times\mathbf{u}_w^g$ [*Tremblay and Mysak*, 1997], where $\mathbf{u}_w^g$ is the geostrophic ocean velocity. Following *Zhang and Hibler* [1997], we neglect the advection term $(\mathbf{u}\cdot\nabla)\mathbf{u}$. This term only becomes important for length scales of a few kilometers, i.e., not important for this study. The acceleration term $\frac{\partial \mathbf{u}}{\partial t}$ can be important on time scales of an hour or smaller. In the following, we keep this term and quantify its importance in the KE balance. The external air and water stresses acting on the ice are parameterized as quadratic laws as [*McPhee*, 1975]:

$$\tau_\mathbf{a}=\rho_a C_{da}|\mathbf{u}_a^g|\left(\mathbf{u}_\mathbf{a}^\mathbf{g}\cos\theta_a+\mathbf{k}\times\mathbf{u}_\mathbf{a}^\mathbf{g}\sin\theta_a\right) \ , \tag{2}$$

$$\tau_\mathbf{w}=\rho_w C_{dw}|\mathbf{u}-\mathbf{u}_w^g|\left[(\mathbf{u}-\mathbf{u}_w^g)\cos\theta_w+\mathbf{k}\times(\mathbf{u}-\mathbf{u}_w^g)\sin\theta_w\right] \ , \tag{3}$$

where ρ_a and ρ_w are the air and water densities, C_{da} and C_{dw} the air and water drag coefficients, $\mathbf{u}_a^g$ the geostrophic wind, and θ_a and θ_w the wind and water turning angles. The sea-ice velocity is neglected in equation (2) since it is much smaller than geostrophic wind speeds.

In a two thickness-categories model (ice or no ice) [*Hibler*, 1979], the volume (or mass) of ice is characterized by the mean thickness (h) and concentration (A) inside a grid cell. Evolution equations for these variables are needed to close the system of equations since $\boldsymbol{\sigma}=\boldsymbol{\sigma}(h,A)$. The continuity equations are given by

$$\frac{\partial h}{\partial t}+\nabla\cdot(h\mathbf{u})=S_h \ , \tag{4}$$

$$\frac{\partial A}{\partial t}+\nabla\cdot(A\mathbf{u})=S_A \ , \tag{5}$$

where S_h and S_A are thermodynamic source terms. The sea-ice model is coupled thermodynamically to a slab ocean model of 100 m thickness. For details on the thermodynamical processes included in the model, see *Tremblay and Mysak* [1997].

3. Viscous-Plastic Rheology

The term $\nabla\cdot\boldsymbol{\sigma}$ in (1) is referred to as the rheology term. It depends on the mechanical properties of the ice and is defined by the constitutive law relating the internal stresses to the deformations (strain rates). For VP models, a general viscous-plastic constitutive law is given by the Reiner-Rivlin stress relation [e.g., *Smith*, 1993]:

$$\sigma_{ij}=-\frac{P}{2}\delta_{ij}+(\zeta-\eta)\dot{\epsilon}_{kk}\delta_{ij}+2\eta\dot{\epsilon}_{ij} \ , \quad i,j=1,2 \ , \tag{6}$$

where σ_{ij} represents the stress acting in the j direction on a surface area with unit normal in the i direction, with $i,j=\{x,y\}$, δ_{ij} is the Kronecker delta, ζ and η the bulk and shear viscosity coefficients, $\dot{\epsilon}_{ij}=\frac{1}{2}\left(\frac{\partial u_i}{\partial x_j}+\frac{\partial u_j}{\partial x_i}\right)$ are the component of the strain rate tensor and repeated indices indicate summation. The ice strength in isotropic compression P depends on the ice concentration and thickness as [*Hibler*, 1979]:

$$P=P^*\,h\exp\left[-C(1-A)\right] \ , \tag{7}$$

where $P^*=27.5\times10^3$ Nm^{-2} is the ice compressive strength parameter and $C=20$ is an empirical ice concentration parameter. The formulations for ζ and η depend on the particular yield curve used. For the elliptical yield curve and normal flow rule, the viscous coefficients are defined as [*Hibler*, 1979]:

$$\zeta = \frac{P}{2\Delta} \ , \tag{8}$$

$$\eta = \frac{\zeta}{e^2} \ , \tag{9}$$

with $\Delta = \left[(\dot{\epsilon}_{11}^2 + \dot{\epsilon}_{22}^2)(1+e^{-2}) + 4e^{-2}\dot{\epsilon}_{12}^2 + 2\dot{\epsilon}_{11}\dot{\epsilon}_{22}(1-e^{-2})\right]^{1/2}$; $e = 2$ is the aspect ratio of the ellipse. To avoid singularities as $\Delta \to 0$, the viscous coefficients are capped using the continuous formulation developed by *Lemieux and Tremblay* [2009]:

$$\zeta = \zeta_{max} \tanh\left(\frac{P}{2}\Delta^{-1}\zeta_{max}^{-1}\right) \ , \tag{10}$$

with $\zeta_{max} = (2.5 \times 10^8)P$ and η still defined by (9). When viscous coefficients are capped, the stress states are no longer plastic, but they lie on a concentric ellipse inside the yield curve (viscous stress states). Simulations were also repeated using the original capping suggested by *Hibler* [1979]. The conclusions presented in the paper are not affected by the choice of capping.

4. Kinetic Energy Equation

The kinetic energy per unit area, K, can be written as:

$$K = \frac{1}{2}\rho_i h\left(u^2 + v^2\right) = \frac{1}{2}\rho_i h(\mathbf{u}\cdot\mathbf{u}) \ , \tag{11}$$

and its local rate of change as:

$$\frac{\partial K}{\partial t} = \frac{1}{2}\rho_i(\mathbf{u}\cdot\mathbf{u})\frac{\partial h}{\partial t} + \mathbf{u}\cdot\left(\rho_i h \frac{\partial \mathbf{u}}{\partial t}\right) \ . \tag{12}$$

The first and second terms on the right-hand side of equation (12) represent the change in inertia $\left(\text{or mass; } \frac{\partial h}{\partial t}\right)$ and acceleration $\left(\frac{\partial \mathbf{u}}{\partial t}\right)$. Substituting the continuity (4) and momentum (1) equations in the first and second terms of equation (12), respectively, we obtain the kinetic energy balance for a 2-D continuum:

$$\mathrm{p_k} = \mathrm{p_h} + \mathrm{p_a} + \mathrm{p_w} + \mathrm{p_i} + \mathrm{p_g} \ , \tag{13}$$

where $\mathrm{p_k} = \partial K/\partial t$ is the rate of change of KE per unit area, $\mathrm{p_h} = \frac{1}{2}\rho_i(\mathbf{u}\cdot\mathbf{u})\frac{\partial h}{\partial t} = \frac{1}{2}\rho_i(\mathbf{u}\cdot\mathbf{u})[S_h - \nabla\cdot(h\mathbf{u})]$ is the power due to the change in inertia (positive when the mean thickness is increasing), $\mathrm{p_a} = \mathbf{u}\cdot\tau_a$ is the power input by the surface wind stresses, $\mathrm{p_w} = -\mathbf{u}\cdot\tau_w$ is the rate of work done by the ocean drag, $\mathrm{p_i} = \mathbf{u}\cdot(\nabla\cdot\boldsymbol{\sigma})$ is the rate of work done by the internal stresses (see section 4.1 for details), and $\mathrm{p_g} = -\rho_i hg(\mathbf{u}\cdot\nabla H) = -\rho_i hf\left(uv_w^g - vu_w^g\right)$ is the power generated by gravity when ice is drifting on a sloping sea surface (positive when ice is accelerating by moving downslope on the sea surface). The Coriolis term does not appear in the energy balance since the resulting acceleration is perpendicular to the velocity vector. Note that the power due to the change in inertia accounts for both the changes in h due to thermodynamical processes (S_h) and the changes in h due to mechanical processes $(-h(\nabla\cdot\mathbf{u}))$. This KE equation (13) has also been derived by *Coon and Pritchard* [1979] and *Pritchard* [1981], except for the previously neglected change-in-inertia term.

4.1. The Internal-Stress Power

The internal-stress power, $\mathrm{p_i} = \mathbf{u}\cdot(\nabla\cdot\boldsymbol{\sigma})$, is the rate of work done on the ice by the internal stresses that leads to a change of its kinetic energy (KE). We define $\mathrm{p_i}$ as negative when internal stresses are doing work to deform the sea ice (i.e., energy dissipation during deformations). Following *Coon and Pritchard* [1979], we express $\mathbf{u}\cdot(\nabla\cdot\boldsymbol{\sigma})$ as the difference between the total rate of work done by σ and the deformation rate of

work that dissipates energy and/or affects the potential energy of the system [see also *Kundu and Cohen*, 2008]. Using tensor notation (where repeated indices indicate a sum), this can be written as:

$$\begin{aligned} \mathrm{p_i} &= \mathbf{u}\cdot(\nabla\cdot\boldsymbol{\sigma}) = u_i(\partial_j\sigma_{ij}) \\ &= \left[u_i(\partial_j\sigma_{ij}) + \sigma_{ij}(\partial_j u_i)\right] - \sigma_{ij}(\partial_j u_i) \\ &= \nabla\cdot(\mathbf{u}\cdot\boldsymbol{\sigma}) - \sigma_{ij}(\partial_j u_i) \\ &= \underbrace{\nabla\cdot(\mathbf{u}\cdot\boldsymbol{\sigma})}_{\mathrm{p_{lat.transm}}} \underbrace{-\,\mathrm{tr}\,(\dot{\epsilon}\boldsymbol{\sigma})}_{\mathrm{p_{pot}}+\mathrm{p^R_{fric}}+\mathrm{p^S_{fric}}} , \end{aligned} \tag{14}$$

where $\mathrm{tr}\,(\dot{\epsilon}\boldsymbol{\sigma}) = \sigma_{ij}\dot{\epsilon}_{ij}$.

In equation (14), the term $\nabla\cdot(\mathbf{u}\cdot\boldsymbol{\sigma})$ is the total rate of work done by the internal stresses. It can also be considered as the lateral transmission of energy (or stress flux divergence) through ice boundaries as a result of local imbalance between energy input by air stresses and energy dissipated by ocean drag, assuming the other power terms are small [*Coon and Pritchard*, 1979]. Using the divergence theorem, the term $\nabla\cdot(\mathbf{u}\cdot\boldsymbol{\sigma})$, averaged over any arbitrary 2-D region $\mathcal{R}$ of area A and contour C, can be written as:

$$\frac{1}{A}\int\!\!\int_{\mathcal{R}} \nabla\cdot(\mathbf{u}\cdot\boldsymbol{\sigma})\,dA = \frac{1}{A}\oint_C (\mathbf{u}\cdot\boldsymbol{\sigma})\cdot\hat{n}\,dl = \frac{1}{A}\oint_C \mathbf{u}\cdot(\boldsymbol{\sigma}\cdot\hat{n})\,dl \ , \tag{15}$$

where $\hat{n}$ is a unit normal vector perpendicular to the boundary of $\mathcal{R}$, $\boldsymbol{\sigma}\cdot\hat{n}$ is the stress acting on the contour C, and the line integral represents the rate of work transmitted through the contour C. Taking $\mathcal{R}$ to be each grid cell in a numerical domain, the term $\nabla\cdot(\mathbf{u}\cdot\boldsymbol{\sigma})$ represents the power laterally transmitted by the internal stresses through ice-covered cell boundaries. In the following, we use $\nabla\cdot(\mathbf{u}\cdot\boldsymbol{\sigma}) = \mathrm{p_{lat.transm}}$.

The term $\mathrm{tr}\,(\dot{\epsilon}\boldsymbol{\sigma})$ in equation (14) includes the rate of work done to change the potential energy ($\mathrm{p_{pot}}$) and the rate of work dissipated in friction by the internal stresses ($\mathrm{p_{fric}} = \mathrm{p^R_{fric}} + \mathrm{p^S_{fric}}$). It is also called the deformation rate of work [*Kundu and Cohen*, 2008], since it assumes nonzero values when ice is deforming. Changes in potential energy occur during ridging when the center of mass of the deformed floes changes position. Energy is dissipated by the internal stresses as frictional losses both in ridging ($\mathrm{p^R_{fric}}$—*Rothrock* [1975]) and shearing ($\mathrm{p^S_{fric}}$—*Pritchard* [1981]) plastic deformations. In viscous-plastic models, energy is also dissipated by the irreversible viscous creep used to approximate small elastic deformations. Assuming ice as an isotropic material with coinciding principal axes of stress and strain rate, the term $\mathrm{tr}\,(\dot{\epsilon}\boldsymbol{\sigma})$ can be written as a function of the stress and strain rate invariants as $\mathrm{tr}\,(\dot{\epsilon}\boldsymbol{\sigma}) = \dot{\epsilon}_I\sigma_I + \dot{\epsilon}_{II}\sigma_{II}$ (see Appendix A). Since $\dot{\epsilon}_I = 0$ in pure shear deformations and $\dot{\epsilon}_{II} = 0$ in biaxial convergence/divergence, the terms $\dot{\epsilon}_I\sigma_I$ and $\dot{\epsilon}_{II}\sigma_{II}$ can be thought of as the deformation rates of work done by the internal stresses during ridging/opening and shearing respectively. These can also be expressed explicitly in terms of the bulk (ζ) and shear (η) viscosity. Using the general form of the viscous constitutive law as $\sigma_{ij} = -\frac{P}{2}\delta_{ij} + (\zeta - \eta)(\dot{\epsilon}_{kk})\delta_{ij} + 2\eta\dot{\epsilon}_{ij}$, we get:

$$\begin{aligned} -\mathrm{tr}\,(\dot{\epsilon}\boldsymbol{\sigma}) &= (-\dot{\epsilon}_I\sigma_I) + (-\dot{\epsilon}_{II}\sigma_{II}) \\ &= \left(\mathrm{p_{pot}} + \mathrm{p^R_{fric}}\right) + \left(\mathrm{p^S_{fric}}\right) , \end{aligned} \tag{16}$$

where,

$$\mathrm{p_{pot}} = \frac{P}{2}(\nabla\cdot\mathbf{u}) \ , \tag{17}$$

$$\mathrm{p^R_{fric}} = -\zeta(\nabla\cdot\mathbf{u})^2 = -\zeta\dot{\epsilon}_I^2 \ , \tag{18}$$

$$\mathrm{p^S_{fric}} = -\eta\left[2\left(\dot{\epsilon}_{11}^2 + \dot{\epsilon}_{22}^2 + 2\dot{\epsilon}_{12}^2\right) - (\nabla\cdot\mathbf{u})^2\right] = -\eta\dot{\epsilon}_{II}^2 \ . \tag{19}$$

The formulations for the energy dissipation given above are general and apply to any VP rheology. We can further distinguish whether the frictional dissipation in ridging ($\mathrm{p^R_{fric}}$) and shearing ($\mathrm{p^S_{fric}}$) is associated with

plastic ($p^R_{fric,plast}$ and $p^S_{fric,plast}$) or viscous deformations ($p^R_{fric,visc}$ and $p^S_{fric,visc}$) by imposing a criterion on Δ, a measure of the magnitude of the deformation. The viscous dissipation criterion can then be written as

$$\begin{aligned} \Delta \leq \Delta_c &: \text{viscous deformation} \\ \Delta > \Delta_c &: \text{plastic deformation} \end{aligned} , \tag{20}$$

where Δ_c is the critical deformation size. We define Δ_c as the deformation size for which the viscous coefficients reach their maximum values when using the elliptical yield curve and the capping of *Hibler* [1979], i.e., when $\zeta = \zeta_{max} = (2.5 \times 10^8)P$, or equivalently:

$$\Delta_c = \frac{P}{2\zeta_{max}} = \frac{P}{2 \times (2.5 \times 10^8)P} = \left(2 \times 10^{-9}\right) \mathrm{s}^{-1} . \tag{21}$$

This definition (21) of the critical deformation size depends on the choice of the maximum viscous coefficients and it can therefore take different values depending on the VP model used. Note that frictional dissipation has always the same form as in equations (18) and (19) regardless of whether the deformation is plastic or viscous.

Summing up, the internal-stress power can be written as:

$$p_i = p_{lat.transm} + p_{pot} + p^R_{fric,plast} + p^R_{fric,visc} + p^S_{fric,plast} + p^S_{fric,visc} , \tag{22}$$

where $p^R_{fric,plast}$, $p^R_{fric,visc}$, $p^S_{fric,plast}$, and $p^S_{fric,visc}$ are the plastic and viscous frictional losses in ridging and shearing, respectively.

5. Numerical Scheme and Forcing Fields

The momentum equation is discretized on the Arakawa C-grid and solved numerically using a Jacobian Free Newton-Krylov (JFNK) method [*Lemieux et al*., 2010]. In each Newton Loop (NL) of the JFNK solver (outer loop iterations in *Lemieux and Tremblay* [2009]), the linearized set of equations are solved iteratively using the preconditioned Generalized Minimum RESidual (GMRES) method [*Lemieux et al*., 2008]. The nonlinear water drag and viscous coefficients are updated and the process is repeated with added NL iterations until convergence or until a maximum number of NL iterations (NL_{max}) is reached. Here we assume convergence is reached when the residual norm of the solution has reached a certain tolerance (i.e., when $residual \leq tolerance$). In section 6.5, we study the dependence of each term in the KE balance on the level of convergence of the nonlinear solver. The reader is referred to *Lemieux et al*. [2008] and *Lemieux et al*. [2010] for more details on the numerical scheme.

The model is forced with atmospheric fields from the National Centers for Environmental Prediction/National Center for Atmospheric Research (NCEP/NCAR) reanalyzes. Linear interpolation between the two closest 6 hourly geostrophic wind fields is used to calculate the wind forcing at any time level. The monthly climatological ocean temperatures are specified at the model's open boundaries from the Polar Science Center Hydrographic Climatology (PHC 3.0) [*Steele et al*., 2001]. The yearly mean oceanic currents are obtained by solving the Navier-Stokes equation in steady state (without advection) assuming a 2-D nondivergent velocity field and using a 30 years climatological forcing wind stress field.

6. Results

The model is first spun-up for 10 years (1970–1979) using 1 m ice thickness and 100% ice concentration as initial conditions. The numerical domain consists of a Cartesian grid superimposed on a polar stereographic projection of the physical domain [see *Tremblay and Mysak*, 1997, Figure 8]. We perform a control run on a 40 km grid for 25 years (1980–2004) with a 1 h time step and a maximal number of Newton loop iterations of $NL_{max} = 500$ (residual norm: $\mathcal{O}(10^{-5})$). Additional simulations on a 10 km grid and with $NL_{max} = 500, 50,$

and 5 are also presented to study the effects of convergence and of spatial resolution on the KE balance (sections 6.3 and 6.5).

All the terms in the KE balance are computed as scalars at the center of all ice-covered grid cells ($A > 0.15$) at the end of each time step. The terms are then averaged in time and/or space to form the averaged quantities presented in the following sections. All terms, except p_a, p_w, and $p_{lat.transm}$, are formed directly at the grid center by linear interpolation (from the two nearest *u* or *v* locations) of quantities not already defined at the center of the cells, e.g.,

$$p_{k,ij} = \frac{\partial}{\partial t}\left(\frac{1}{2}\rho_i h_{ij}\left[\left(\frac{u_{ij}^2+u_{i+1,j}^2}{2}\right)+\left(\frac{v_{ij}^2+v_{i,j+1}^2}{2}\right)\right]\right)$$

The terms p_a, p_w, and $p_{lat.transm}$ are instead formed at the u and *v* locations on the C-grid and then averaged to the grid center to reduce the stencil of the calculation, e.g.,

$$p_{a,ij} = \left[\frac{u_{ij}\tau_{ax,ij}+u_{i+1,j}\tau_{ax,i+1,j}}{2}\right]+\left[\frac{v_{ij}\tau_{ay,ij}+v_{i,j+1}\tau_{ay,i,j+1}}{2}\right]$$

While the choice of the numerical stencils used to compute the terms of the KE balance can affect the residual error in the KE balance, it does not affect the conclusions of the present study.

6.1. Arctic-Averaged Seasonal Cycle

The main balance in the Arctic-averaged monthly climatology (25 years) of the power terms in equation (13) is between the power input by the surface wind stress, the power dissipated by the water drag and the power dissipated by the internal stresses (Figure 1). Note that the internal stress term appears as a dissipative term on a domain average but can take both positive and negative values locally (see section 6.4). All first-order terms are larger in winter and smaller during summer. In the mid-late summer, ice-ice interactions are small and all energy input is dissipated by the water drag. On an annual mean, the water drag dissipates 87% of the energy input by the air stress and the internal stress term dissipates the remaining 13%. Given the interannual variability, this is in agreement with values of the 7 years study of *Steele et al.* [1997].

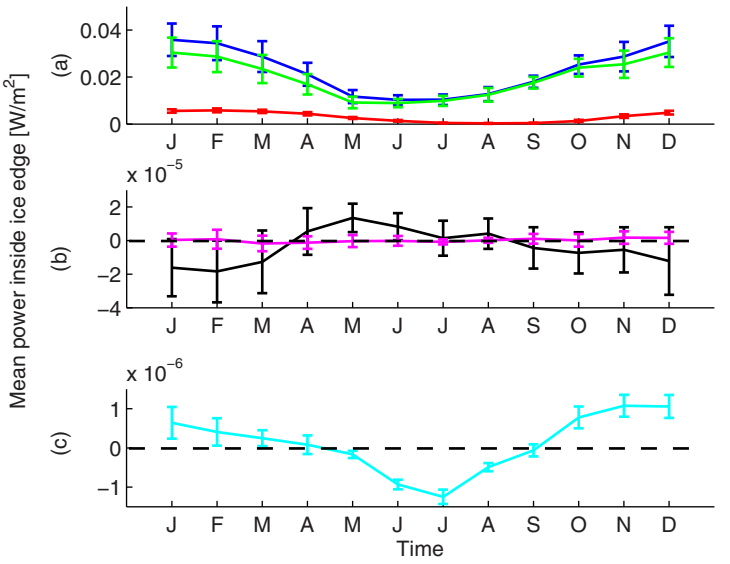

Figure 1. Arctic-mean monthly climatology (25 years) and standard deviations of (a) p_a (blue), $-p_w$ (green), and $-p_i$ (red); (b) p_k (magenta) and p_g (black); and (c) p_h (cyan)—see section 4 for the definition of each term. The spatial average is done for all points within the ice edge ($A > 0.15$). The annual mean values for each term (in W/m^2) are p_a : 0.0227, $-p_w$: 0.0198, $-p_i$: 0.0029, p_k : 1×10^{-7}, p_g : -4×10^{-6}, and p_h : 1×10^{-7}. The dashed black lines in Figures 1b and 1c are the zero line.

The second-order and third-order terms in the KE balance are 1–10 thousand times smaller than the dominant terms and include the power generated by gravity, $\langle p_g \rangle$, the temporal change of the total KE, $\langle p_k \rangle$, and the power associated with changes in inertia (or mass), $\langle p_h \rangle$ (Figure 1b—$\langle\rangle$ denotes the Arctic average). The magnitude of $\langle p_g \rangle$ is minimal in spring/summer and maximal in winter when the Beaufort Gyre is well established. $\langle p_h \rangle$ follows a seasonal cycle with positive values during the winter and negative values during summer corresponding to the thermodynamical cycle of growth and melt of ice. These three terms are equally small in the local KE balance derived from

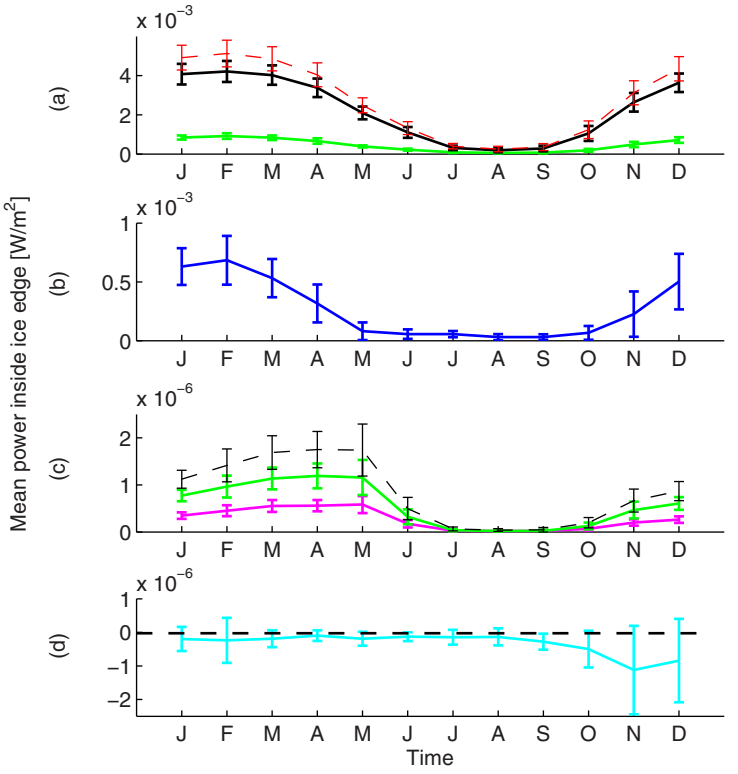

Figure 2. Arctic-mean monthly climatology (25 years) and standard deviations of (a) $-p^R_{fric,plast}$ (green), $-p^S_{fric,plast}$ (black), and $-p_{fric,plast}=-(p^R_{fric,plast}+p^S_{fric,plast})$ (dashed red); (b) $-p_{pot}$ (blue); (c) $-p^R_{fric,visc}$ (magenta), $-p^S_{fric,visc}$ (green) and $-p_{fric,visc}=-(p^R_{fric,visc}+p^S_{fric,visc})$ (dashed black); and (d) $-p_{lat.transm}$ (cyan)—see section 4 for the definition of each term. The spatial average is done for all points within the ice edge ($A>0.15$). The annual mean values for each term (in W/m^2) are $-p^R_{fric,plast}$: 0.0004, $-p^S_{fric,plast}$: 0.0023, $-p_{pot}$: 0.0002, $-p^R_{fric,visc}$: 2×10^{-7}, $-p^S_{fric,visc}$: 6×10^{-7}, and $-p_{lat.transm}$: -3×10^{-7}. The dashed black line in Figure 2d is the zero line.

monthly mean and snapshot fields and will not be discussed in later sections.

The rate of work done by the internal stress term, $\langle p_i \rangle$, is dominated by the frictional dissipation during plastic shearing deformations ($\langle p^S_{fric,plast} \rangle$) that dissipates 77% of the total $\langle p_i \rangle$, followed by the frictional dissipation in plastic ridging deformations ($\langle p^R_{fric,plast} \rangle$) and by the power due to changes in the potential energy ($\langle p_{pot} \rangle$), dissipating 15% and 9% of $\langle p_i \rangle$ respectively (Figure 2). Since $\langle p_{pot} \rangle$ transfers KE into potential energy stored in irreversible plastic ridging deformations, it follows closely the seasonal variations of $\langle p^R_{fric,plast} \rangle$. The importance of each power term composing $\langle p_i \rangle$ is dependent on the choice of the ellipse aspect ratio. The value $e=2$ was derived from strain rate measurements [*Hibler*, 1974, 1979] and supported from observations of opening/closing distributions as functions of the ratio of divergence to shear invariants [*Stern et al.*, 1995]. For $e>1$, the shear strength of the ice is less than the ice strength in isotropic compression, offering less resistance to shear deformations than ridging. For instance, an ellipse ratio of 2 makes the shear viscosity four times smaller than the bulk viscosity (see equations (8) and (9)), but frictional dissipation by the internal stresses is dominated by the shear strain rates and much less by the viscous coefficients (results not shown).

The dissipation by viscous deformations, $\langle p_{fric,visc} \rangle = \langle p^R_{fric,visc} \rangle + \langle p^S_{fric,visc} \rangle$, is roughly a 1000 times smaller than the domain-averaged dissipation by plastic deformations (Figure 2c). This suggests that dissipation by the nonphysical viscous deformations is negligibly small in the KE balance. Whether this holds in the local nonaveraged balance will be discussed in the next sections.

The power laterally transferred by the internal stresses during deformations, $\langle p_{lat.transm} \rangle$, has a nearly zero domain average during the whole year (Figure 2d). As shown by *Pritchard* [2005], the integral of the term $p_{lat.transm}$ on the entire domain should indeed be zero when the sea-ice velocity is taken to be zero on the boundaries. However, the term $p_{lat.transm}$ is a first-order term locally and generally redistributes KE input from the wind to LFKs where dissipation occurs by friction and changes in potential energy (see sections 6.2 and 6.4).

6.2. Local Monthly Averaged KE Balance

We present results for the local March and September KE balance for the year 1992. While there is interannual variability in the KE balance (e.g., associated with the Arctic or North Atlantic Oscillation), the conclusions drawn from a specific year are robust. The Arctic-mean residual error in the monthly mean KE balance,

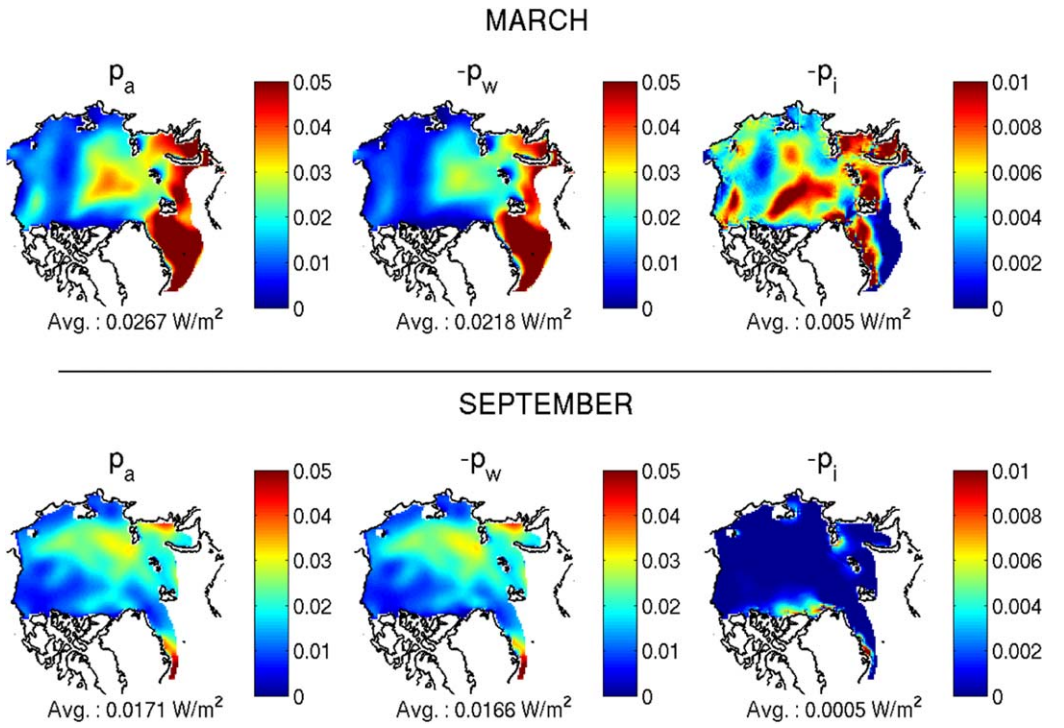

Figure 3. Monthly mean of the first-order terms in the KE balance (in W/m^2) for March and September 1992—see section 4 for the definition of each term. We show $-p_w$ and $-p_i$ for ease of comparison with the power input, p_a. Note that the internal stress term, p_i, can sometimes act as a source of KE ($-p_i > 0$), but we cap $-p_i$ to zero to keep the color bar consistent between those of p_a and $-p_w$.

calculated as $|p_k - (p_a + p_w + p_i + p_g + p_h)|$, is approximately 2% of the Arctic-averaged monthly mean energy input (p_a) in March and less than 1% in September.

The power input by winds and the power dissipated by the oceanic drag are the two largest contributions in the monthly mean balance (both in March and September—Figure 3) with powers on the order of 10^{-2} W/m^2 in the central Arctic in agreement with values calculated by *Coon and Pritchard* [1979]. Generally, the spatial pattern of p_w follows that of p_a with local differences in intensity almost entirely compensated by the internal stress term (results not shown). During winter, important ice interactions are present almost everywhere, except at the center of the Beaufort Gyre (where deformations are small) and in the marginal ice zone in the Eurasian basin (where ice is in free drift). Regions of high dissipation by shear strain rates are present at the outer edge of the Beaufort Gyre, adjacent to the less-mobile sea ice north of the Canadian Arctic Archipelago (CAA). In summer, the mean value of p_i drops by a factor of approximately 10. Thin ice and open water in the pack allows ice floes to move more freely in the central Arctic reducing the transmission of stress between the floes [*Richter-Menge*, 1997] and the importance of p_i in this region decreases.

The first-order terms in the local internal stress term p_i for both March and September are $p_{lat.transm}$, p_{pot}, and $p_{fric,\,plast} = p^R_{fric,\,plast} + p^S_{fric,\,plast}$ (Figures 4 and 5). The spatial distributions of $p_{lat.transm}$ and of the total internal stress term are very similar, indicating that the main role of the internal stresses in the KE balance is not only the dissipation of energy during deformations, but also the redistribution of energy laterally within the pack. In fact, $p_{lat.transm}$ redistributes energy away from the input locations $(p_{lat.transm} < 0)$ to regions of deformation $(p_{lat.transm} > 0)$ where it is used in frictional dissipation and/or stored as potential energy (also observed with EP model—see *Pritchard* [1981]). The power due to changes in potential energy during converging/diverging deformations (p_{pot}) also acts as a redistributive term, but this time between KE and potential energy during deformations. During ridging $(\nabla \cdot \mathbf{u} < 0)$, p_{pot} is negative and KE is lost to potential energy stored in the ridge. The areas of positive p_{pot} (associated with opening of the pack or $\nabla \cdot \mathbf{u} > 0$) are an artifact of using a normal flow rule jointly with an elliptical yield curve, because P is allowed to be nonzero even when the divergence is positive.

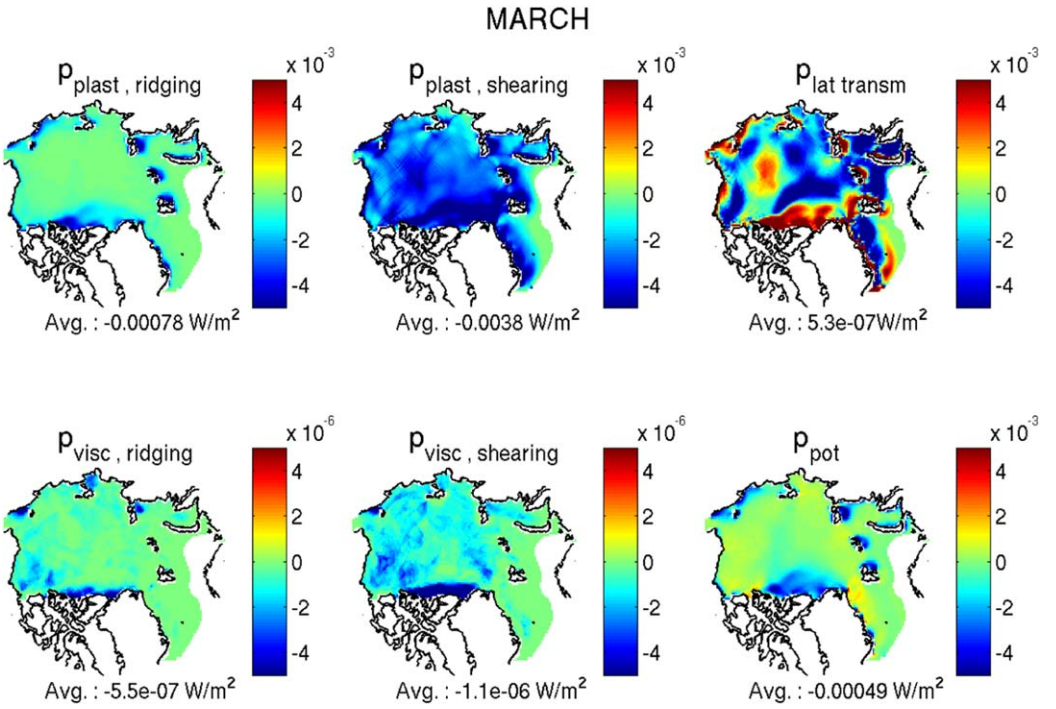

Figure 4. March mean of each term composing p_i (in W/m^2) for the year 1992—see section 4 for the definition of each term.

Highly dissipative plastic ridging deformations occur mainly along the coastlines, while shearing dissipation of the same order of magnitude is present everywhere in the domain. Overall, the average power dissipated by shearing deformations is approximately five times larger than that dissipated by ridging deformations. This is supported by observations from RGPS that show that the shear strain rate invariant $(\dot{\epsilon}_{II})$ is larger than the divergence invariant $(\dot{\epsilon}_{I})$ in most local deformation events in the central Arctic [*Stern et al*., 1995].

In September, p_i is active mostly north of the CAA and in other regions of high sea-ice concentration (e.g., at the entrance of the Kara Sea). This reduced area of ice interaction results in a mean intensity of the plastic dissipation that is approximately 10 times smaller than in March. The change of sign of the term p_{pot} near the CAA from negative in March to positive in September is related to the change in the monthly mean ice drift patterns. In March, the Beaufort Gyre and Transpolar Drift Stream promote converging ice velocity $(p_{pot} < 0)$ north of the CAA, while the cyclonic circulation in September (of that particular year) leads to shearing and diverging motion $(p_{pot} > 0)$ in the same region.

In both seasons, viscous dissipation is approximately a 1000 times smaller than plastic dissipation locally in the monthly averaged fields. There exist regions, however, where ice is most of the time in the viscous regime (e.g., North of the New Siberian Islands, Beaufort Sea, and Lincoln Sea). However, the total monthly mean energy dissipated in these regions is still dominated by the less frequent but more energetic plastic deformations. The VP approximation is therefore appropriate for the monthly time scale at 40 km of spatial resolution.

6.3. Effects of an Increasing Spatial Resolution

Before analyzing the role of each power term from higher-resolution snapshots of the KE balance, we look at the effects of an increasing spatial resolution the KE balance. We run the same model, again for the time period of 1 January 1992 to 31 December 1992, on a 10 km grid with the same time step (1 h) and degree of convergence (NL_{max}=500—residual norm: $\mathcal{O}(10^{-3})$).

The monthly mean KE balance at 10 km spatial resolution (not shown) resemble that of the 40 km run, except that finer structures are visible in all power terms. Some shear lines are now visible in the plastic dissipation in shearing deformations, $p^S_{fric,plast}$, especially around the Beaufort Gyre. The mean error on closing the monthly mean balance for the 10 km run is again about 2% of the Arctic-averaged mean value of the

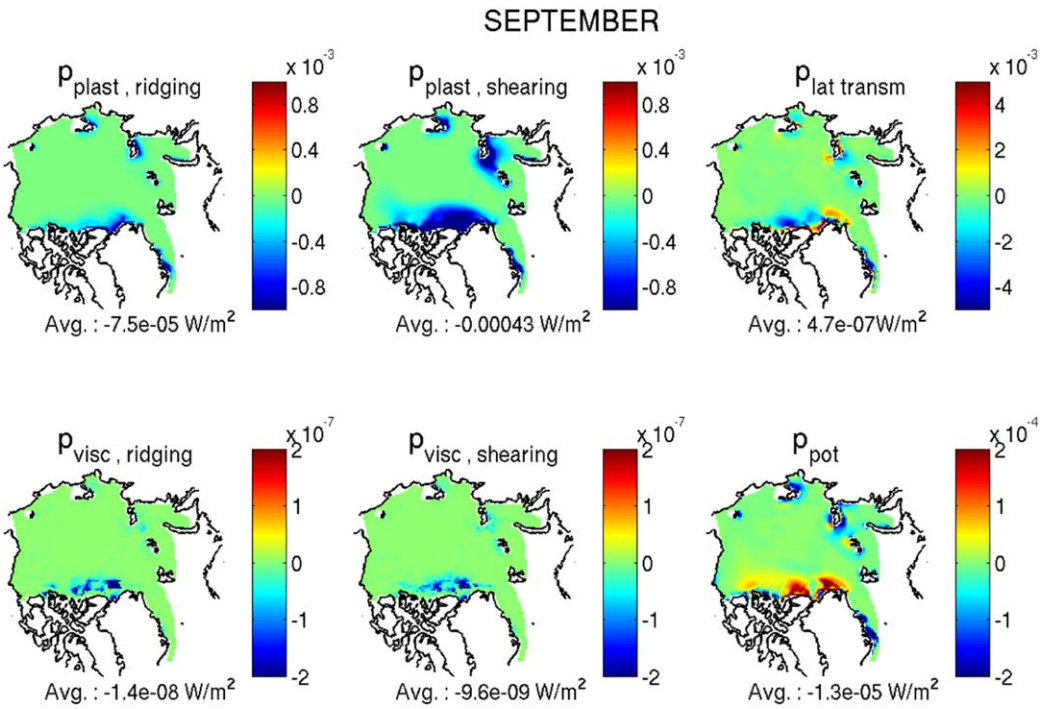

Figure 5. September mean of each term composing p_i (in W/m^2) for the year 1992—see section 4 for the definition of each term.

energy input by the surface winds. Note that in the following, we neglect data from the CAA when performing domain averages to compare with the same domain as in the 40 km resolution run.

During the month of March, the monthly mean ratio of the number of grid points in the viscous and plastic regimes (N_{visc}/N_{plast}) increases from 7% (for the 40 km grid) to 19% on the 10 km grid due to refined LKFs. With increasing resolution, broad deformation lines separate into groups of finer LFKs and new deformation lines also appear (results not shown). The net result is an increased number of grid cells in the viscous regime at the expense of the plastic regime. However, the ratio of the Arctic-averaged monthly mean dissipation in each deformation regime still yields $\langle p_{fric,\,visc}\rangle/\langle p_{fric,\,plast}\rangle \sim 10^{-3}$ because the increment in the viscous energy sink is still small compared to the resulting plastic energy sink. As shown by *Wang and Wang* [2009], the choice of a particular yield curve affects the position and the spatial distribution of the LKFs as the spatial resolution increases. This will affect the ratio of N_{visc}/N_{plast} and the total viscous sink. However, we expect that the viscous dissipation would still be negligible. This is because the stress states scale approximately the same regardless of the VP yield curve used. The ratio $\langle p_{fric,\,visc}\rangle/\langle p_{fric,\,plast}\rangle$ scales as $\langle\dot{\epsilon}_{plast}\rangle/\langle\dot{\epsilon}_{visc}\rangle$ and $\langle\dot{\epsilon}_{visc}\rangle$ must be much smaller than $\langle\dot{\epsilon}_{plast}\rangle$ by definition with all VP yield curves.

At 10 km spatial resolution, the mean surface wind stress is higher due to the cubic spline interpolation of the surface winds used to calculate τ_a. Consequently, direct comparison of the magnitude of the energy sinks in the KE balance between the two spatial resolutions considered is not possible. Instead, we report on the ratio of a particular term in the KE balance and the energy input by the wind ($\langle p_a\rangle$; Figure 6). The results for the 25 years climatological values (mean and standard deviation) obtained from the 40 km model are also presented for reference.

The domain-averaged monthly mean ratios $\langle p_i\rangle/\langle p_a\rangle$ and $\langle p_{fric\,,\,plast}\rangle/\langle p_a\rangle$ for the 10 km run are significantly lower (outside the standard deviation of the 25 years climatology) than the same ratios for the 40 km run during the winter months (Figures 6a and 6b). The relative amount of $\langle p_{fric\,,\,visc}\rangle/\langle p_a\rangle$ is also slightly (not significantly) reduced in winter and is still a 1000 times smaller than $\langle p_{fric\,,\,plast}\rangle$ for all months, suggesting that the VP approximation is appropriate with the 10 km grid (Figure 6c). The ratio of the dissipation by the water drag to the atmospheric input, $\langle p_w\rangle/\langle p_a\rangle$, also increases with spatial resolution to balance the decrease in $\langle p_i\rangle/\langle p_a\rangle$ (Figure 6d). This result is also observed for other years (results not shown).

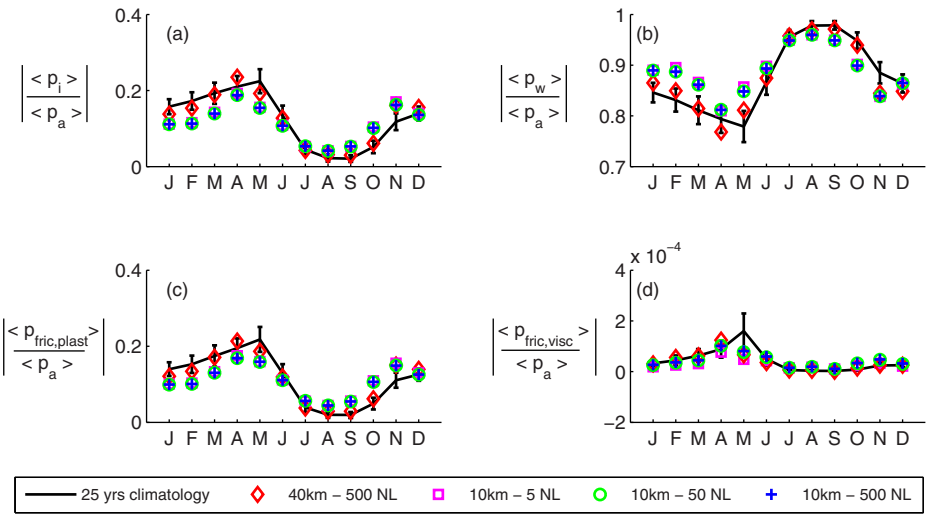

Figure 6. Dissipative terms in the KE balance as a function of the spatial resolution and numbers of Newton loops of the numerical solver. These include: (a) dissipation by the internal stresses, (b) dissipation by the water drag, (c) dissipation in plastic deformations, and (d) dissipation in viscous deformations. Each sink term is normalized with the monthly mean domain averaged atmospheric forcing, $<p_a>$, for comparison between the runs with different forcing. The black line is the climatological mean values (1980–2004) and standard deviations at 40 km spatial resolution.

These differences in the KE balance between the 10 and 40 km simulations suggest that the ice strength in isotropic compression (P^*) should be increased as the spatial resolution of the model is increased. A study of the calibration of the VP model against buoy drift data indeed suggests that a higher value of P^* should be used on a 10 km grid [*Dansereau*, 2011]. *Steele et al.* [1997], studying the sensitivity of the force balance to variations in P^*, showed that increasing the ice strength in isotropic compression considerably increases the internal stress gradients in the pack and slows down the ice drift in winter. We have tested that the amount of small deformations is increased at the expense of larger deformations when P^* is increased in our 10 km model, but that the dissipation by the less frequent large plastic deformations becomes larger. The net effect is an increase of the work done by the internal stresses in winter (even if the ice drift velocity is reduced as P^* increases). Note that changing the value of the ice strength in isotropic compression would also change the deformation patterns and intensity so that the number of points in the viscous and plastic regimes and the total dissipation in both modes would also be affected.

6.4. Snapshots

In this section, we present the KE balance from instantaneous snapshots of each field variables (Figure 7). Snapshots were obtained at every hour for the month of March 1992 for the 10 km run with $NL_{max}=500$ (residual norm: $\mathcal{O}(10^{-3})$ - fully converged). In the following, we focus on the snapshots for 17 March at 1200 universal time coordinated (UTC).

The instantaneous KE balance resembles that of the monthly mean balance for March, except for p_k and p_g that can reach values as large as 1 order of magnitude smaller than the magnitude of the internal stress term for certain time levels (results not shown). The two main energy sinks in the pack are again the water drag (p_w) and the internal ice stress term (p_i). On average inside the pack, the water drag dissipates ~80% of the energy input by p_a. The remaining 20% of the energy input by the wind is transferred and dissipated by the internal stress term in regions of imbalance between p_a and p_w (Figures 7c and 7d). In regions where the winds are small, the dissipation by the water drag exceeds the input of energy locally and the internal stresses act also as a source of energy in those regions. Input of energy by the internal stress term results from an imbalance in the lateral energy transfer from regions of extra energy input $(|p_a|-|p_w|>0)$ to regions where the intensity of the water drag dissipation is greater than that of p_a. This is achieved by the term of lateral transmission of energy ($p_{lat.transm}=\nabla\cdot(\mathbf{u}\cdot\boldsymbol{\sigma})$—Figure 7e).

The role of $p_{lat.transm}$ is well illustrated in the instantaneous KE balance: it redistributes the energy input by the wind toward smaller-scales structures (LKFs) within the pack. The LKFs are clearly defined in the snapshot of $p_{lat.transm}$ by lines of positive transmission of energy (indicating energy being transferred to the

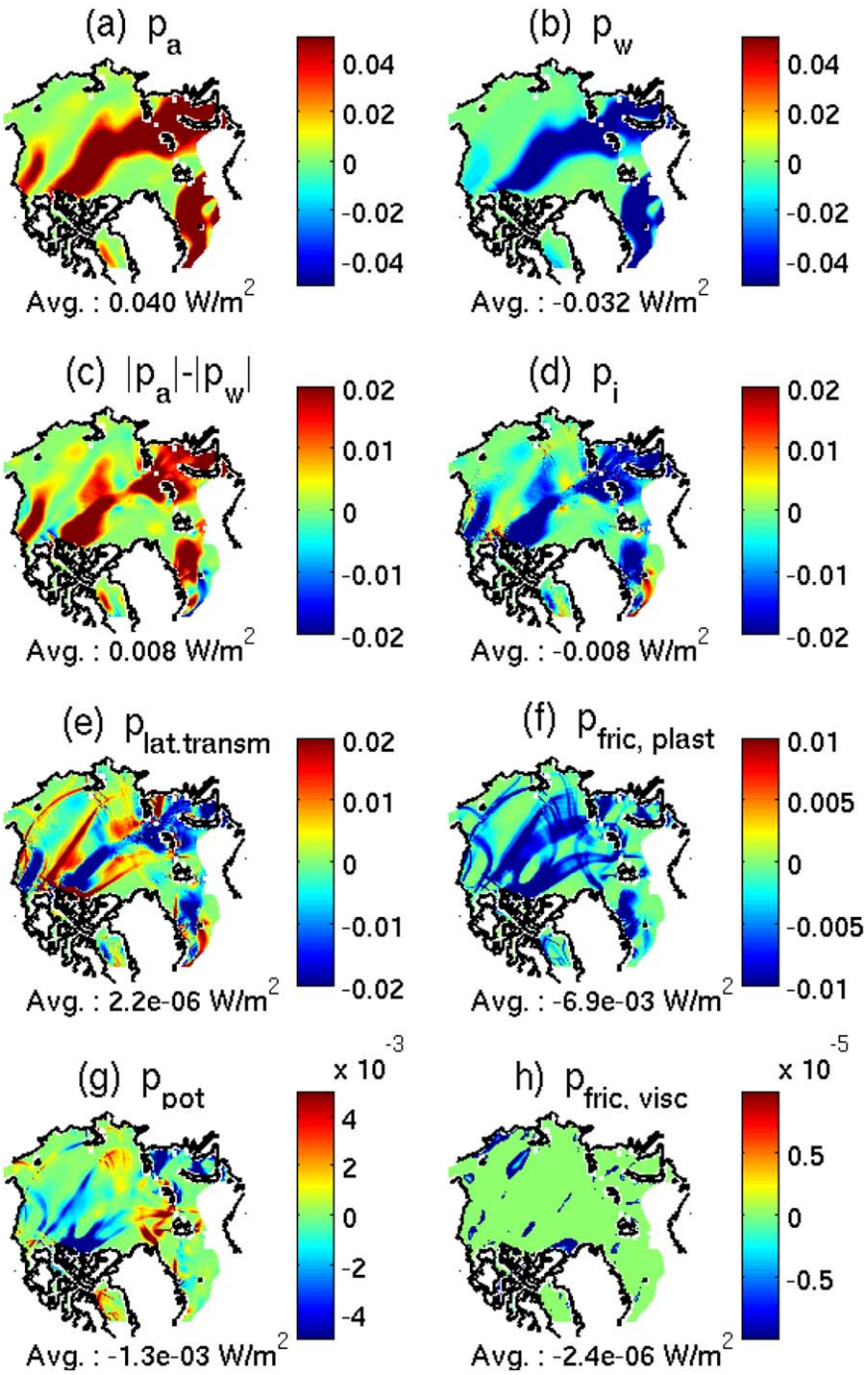

Figure 7. Snapshots of the sources and sinks of energy in the KE balance and in the internal stress term (in W/m^2) with a spatial resolution of 10 km and $NL_{max}=500$ on 17 March 1992 1200 UTC.

LKFs) that are collocated with large area of plastic dissipation (Figure 7e and 7f). Note that, the LKFs are no longer visible in the resulting work by the internal stresses because most of the frictional dissipation is balanced by $p_{lat.transm}$. Along LKFs, the energy is in fact mainly dissipated via frictional dissipation in plastic deformations, but a smaller fraction (up to half of that by $p_{fric, plast}$) is dissipated by the potential energy sink (p_{pot}) in ridging deformations. On a domain average, the plastic dissipation accounts for 85% of the total dissipation by the internal stresses, while p_{pot} accounts for the remaining 15%. The instantaneous Arctic-averaged frictional dissipation in shearing is still five times larger than that in ridging (not shown) as seen in the monthly mean KE balance. Note that there are some regions of plastic dissipation where

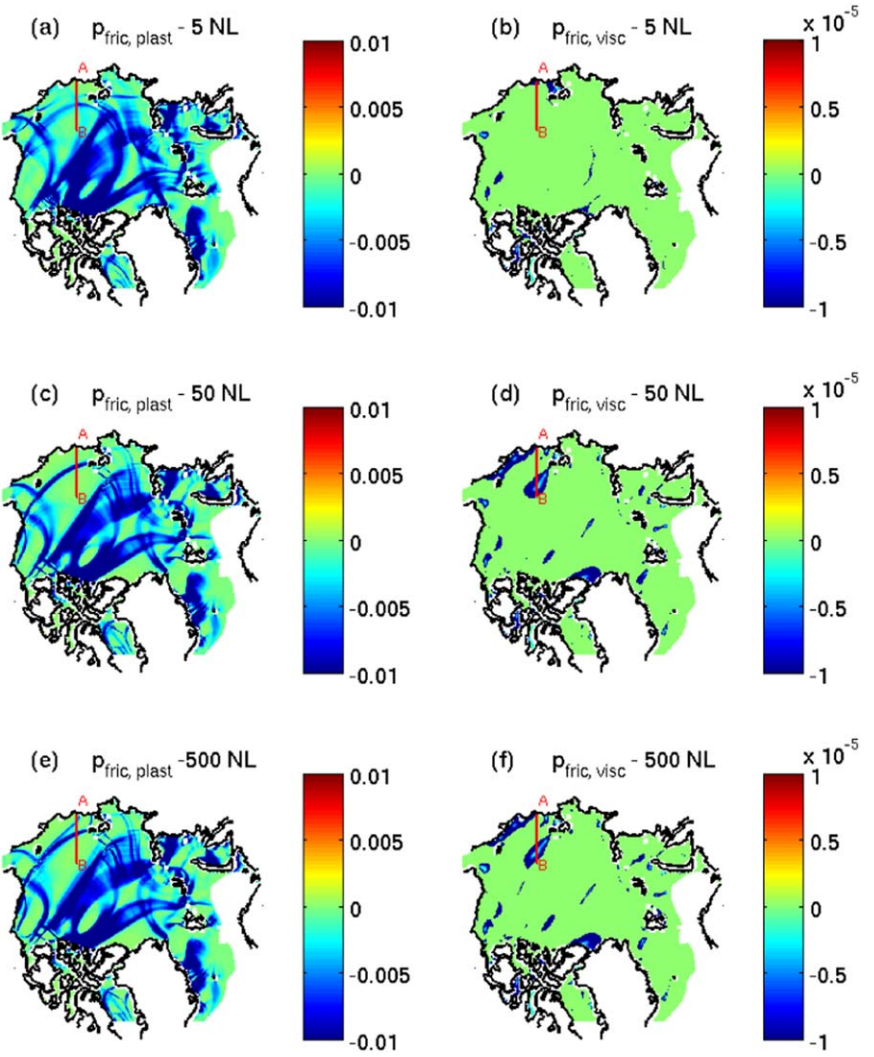

Figure 8. Snapshots of plastic and viscous frictional dissipation (in W/m^2) for the 10 km spatial resolution model on 17 March 1992 1200 UTC, for (a and b) 5 NL, (c and d) 50 NL, and (e and f) 500 NL. Results along the A-B transect are shown in Figure 9.

$p_{lat.transm}$ is also transferring energy away from the deformation locations. In that case, the energy input by the atmospheric wind is larger than the amount of energy dissipated by the water drag and by the plastic dissipation locally, such that the extra input energy is being redistributed elsewhere in the domain by $p_{lat.transm}$.

The ratio of the number of points in the viscous regime to that in the plastic regime (N_{visc}/N_{plast}) for this particular time level is of 14% which is representative of the monthly mean field. As expected, instantaneous viscous frictional dissipation occurs in between LKFs and is again approximately a 1000 times smaller than plastic frictional dissipation (locally and domain averaged). This confirms that the VP approximation is also appropriate on an instantaneous time scale for this model.

6.5. Effects of the Degree of Convergence of the Numerical Solver

We now run the same 10 km resolution model (from 1 January 1992 to 31 December 1992—1 h time step) with different levels of numerical convergence, including $NL_{max}=500$ (from previous section; residual norm: $\mathcal{O}(10^{-3})$ - fully converged), $NL_{max}=50$ (residual norm: $\mathcal{O}(10^{0})$ - solver converging on 14% of the time levels) and $NL_{max}=5$ (residual norm: $\mathcal{O}(10^{1})$—solver never converging).

The number of Newton loops of the nonlinear solver does not significantly affect the ratio of the domain means (or intensity) of the terms in the KE balance (Figure 6). In winter, the ratio $\langle p_{fric,visc}\rangle/\langle p_a\rangle$ is slightly

Table 1. Viscous and Plastic Sinks With Different Levels of Numerical Convergence[a]

NL_{max}	5	50	500
N_{visc}/N_{plast}	0.15	0.18	0.18
$\langle p_{fric,visc}\rangle/\langle p_{fric,plast}\rangle$	2.4×10^{-4}	3.3×10^{-4}	3.5×10^{-4}

[a]Relative importance of the viscous and plastic regimes measured by the monthly mean ratio of the number of grid points in each regime (N_{visc}/N_{plast}) and by the ratio of the Arctic-averaged monthly mean dissipation in each regime $\langle p_{fric,visc}\rangle/\langle p_{fric,plast}\rangle$ for March 1992 and for different maximal number of Newton loops (NL_{max}) in the numerical solver (10 km grid).

increased due to the refinement of plastic deformation lines with increased number of NL [see also *Lemieux and Tremblay*, 2009] leading to larger viscous dissipation areas in between the regions of plastic deformation. For this reason, the monthly mean ratio of grid points in the viscous and plastic regime in the month of March is seen to slightly increase with increasing NL_{max} (Table 1). However, the increased amount of viscous points is not enough to significantly affect the ratio of the Arctic-averaged monthly mean viscous and plastic dissipation ($\langle p_{fric,visc}\rangle/\langle p_{fric,plast}\rangle$) and the viscous energy sink stays negligible even in a nonconverged simulation (Table 1).

Increasing the degree of convergence of the simulation results in similar changes as the increase in spatial resolution (section 6.3). With a high number of NL iterations, new deformation lines that were previously nonexistent or merged with other deformation lines can now be resolved and local dissipation in deformations is increased. This can be seen by comparing snapshots (again on 17 March 1992 at 1200 UTC) of the plastic and viscous dissipation term for the three runs (Figure 8). The local intensity of $p_{fric,visc}$ on these snapshots stays about 1000 times smaller than $p_{fric,plast}$ independently of the number of NL. Note that comparison between the local intensity in the three runs is not possible since the input by the atmospheric stress changes with the number of NL via changes in the sea-ice velocity. Taking the local ratio of the terms with the atmospheric forcing is also not appropriate for comparison of the spatial distributions since the energy dissipated locally usually gets transferred by $p_{lat.transm}$ from a different input region (see section 6.4). We can then only discuss qualitatively the differences between the snapshots.

The main effect of the degree of convergence of the numerical solver on energy dissipation is to modify the deformation lines (position and size) as discussed by *Lemieux and Tremblay* [2009]. We illustrate this by sampling the terms of energy dissipation along the transect (A-B—Figure 8) crossing a LKF, for the three 10 km runs (Figure 9). The corresponding results for the 40 km are also included for comparison and the atmospheric input for each run is also presented along the transect. The resulting spatial distributions for p_i are very different, mostly due to changes in the plastic dissipation. In the nonconverged run ($NL_{max}=5$), the shear line crossed by the transect is broad and the plastic dissipation shows two distinct peaks of maximum dissipation. As the number of Newton loop iterations (i.e., level of convergence) increases, the LKF sharpens and the position of its maximum dissipation shifts toward the coastline (point A of the transect). In the fully converged run ($NL_{max}=500$), a second shear line is resolved near point A (Figure 8a) and another distinct peak of plastic dissipation is observed (Figure 9b). The viscous dissipation is maximum

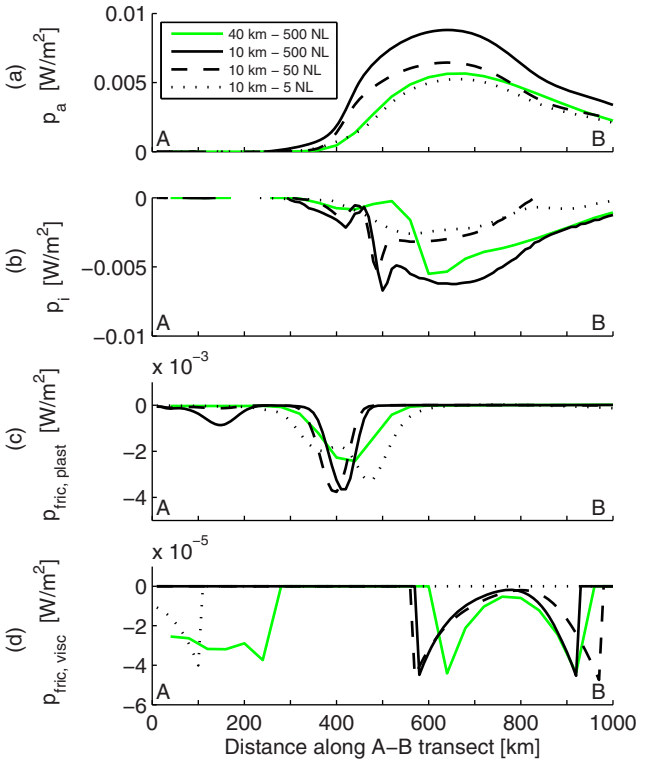

Figure 9. Atmospheric forcing and energy dissipation along the A-B transect of Figure 8: (a) p_a, (b) p_i, (c) $p_{fric,plast}$, and (d) $p_{fric,visc}$.

at the limits between the plastic and viscous regions where the viscous deformations are larger (yet still much smaller than plastic deformations). When NL_{max} is decreased from 500 to 5, the viscous region disappears entirely as a consequence of the plastic deformation line being too diffuse. This illustrates again the migration of stress states from the plastic to the viscous regime with an increased level of convergence.

In this snapshot, the center of the LKF (the highest plastic dissipation point) is offset from the closest maximum of atmospheric input (also observed for other snapshots during the month). In fact, the deformation lines tend to appear on the periphery of the atmospheric input regions, where the shear in ice velocity is larger. The energy input in the pack must therefore be transmitted laterally in the pack for the dissipation to occur in the deformation lines as detailed in the previous section.

It is interesting to note that, along this transect, the distribution of the forcing (p_a) in the converged 40 km run and in the nonconverged 10 km run $(NL_{max}=5)$ are very similar. However, the resulting work from the internal stresses and the dissipation (plastic and viscous) are very different. This illustrates that the forcing is not the only determining factor on energy dissipation, but that the spatial resolution and degree of convergence of the numerical solver are also influential factors.

7. Conclusion

Large plastic deformations in sea ice occur along narrow lines of high strain rates (called linear kinematic features—LKFs), while the surrounding pack undergoes small elastic deformations. To model this mechanical behavior, most current sea-ice models use the viscous-plastic (VP) approximation [*Hibler*, 1979] that considers the small deformations as irreversible viscous deformations. This introduces a nonphysical energy sink in the models, but the gain in numerical efficiency (compared to previous elastic-plastic models) appeared as a sufficient justification for this approximation. The improvements in the numerical efficiency of numerical solvers in the last decade now allow for the solution of the governing equations to be more accurate and on increasingly high-resolution grids. As the spatial resolution is increased, the number of grid points undergoing viscous deformations increase because of the refinement of LKFs [*Wang and Wang*, 2009]. A better converged solution also results in better defined LKFs and a migration of points from the plastic regime toward the viscous regime [*Lemieux and Tremblay*, 2009; *Zhang and Rothrock*, 2000]. In this context, we posed the following questions: is the energy sink associated with the viscous deformation still negligible for better converged and high-resolution sea-ice models? And, what is the relative amount of energy dissipated by each term in the kinetic energy (KE) balance?

For all time scales (annual climatology, monthly means and snapshots) and grid resolution (40 and 10 km) investigated, the VP approximation is shown to be appropriate as viscous dissipation remains a negligible sink of energy (3 orders of magnitude smaller than the leading term) in the KE balance. The climatological seasonal cycle of the KE balance revealed that the internal stress term is a first-order term in the KE balance and that it is mostly active during the winter when the ice-ice interactions are important. The frictional dissipation in plastic deformations along LKFs is found to be the dominant term in forming the total internal stress term, while the potential energy sink is found to be less than half of the magnitude of the plastic dissipation. Annual and monthly averages also showed that frictional dissipation in shearing is about five times bigger than frictional dissipation in ridging. It is indeed easier for large shearing deformations than for large (negative) divergence to occur since the shear strength of the ice is less than its isotropic compressive strength when using an ellipse aspect ratio $e = 2$. A different ellipse ratio as proposed in *Miller et al.* [2005] and *Dumont et al.* [2009] would obviously change the ratio of frictional dissipation in ridging to that in shearing.

The energy input by the atmospheric drag is mainly dissipated by the water drag locally and by the internal stress term along deformation lines over the whole domain. We noted that the dissipation by the internal stresses can occur away from the input locations due to the term of lateral transmission of energy entering in the definition of the internal stress term. Both the frictional dissipation and the lateral transmission are first-order terms and this highlights the fact that terms that appear to be negligible when averaged on the whole domain can be locally important (e.g., the term of lateral transmission of stress). Results from the monthly averaged KE balance show that, large shear deformations are present everywhere on the domain in winter, while ridging deformations dissipating the same amount of energy are found only near the coastlines. In the summer, both the ridging and shearing dissipation are confined to the coastlines and other regions of high ice concentration.

As expected from the refinement of the LKFs at a higher grid resolution, the area of viscous deformations increases with increasing spatial resolution (from 40 to 10 km), but not enough to make a significative change in the averaged amount of viscous dissipation relative to the plastic dissipation. At higher resolution, we found that the ratio of the energy dissipated by the ocean drag to the energy input increases while that of the energy dissipated along deformation lines to the energy input decreases. This suggests that the ice strength in isotropic compression (P^*) should be higher when the resolution increases to maintain the same KE balance (i.e., decrease the water drag dissipation due to reduced sea-ice velocity and increase the internal stress dissipation because of higher viscous coefficients for each deformation). This raises the question of the dependence of the KE balance on the calibration of other model parameters (e.g., drag coefficients and ellipse ratio) and if those are adequate for high-resolution modeling. It is interesting to note that, increasing P^* (and consequently the values of the viscous coefficients) with increasing resolution is in opposition to a fluid behavior where the viscosity need to be decreased as more small-scale dissipating processes are being resolved in the flow (e.g., small-scale eddies in ocean models). Raising the value of P^* for higher-resolution sea-ice models is however consistent with laboratory experiments conducted at smaller scale that also suggest higher compressive/shear strength of a single floe when compared to an aggregate of floes [*Dempsey et al*., 1999].

The KE balance from instantaneous snapshots reveals that the energy input by the wind is dissipated in the pack by the ocean drag (mostly following the same pattern as the energy input) and away from the input locations by small-scale structures (LFKs). The dissipation by the internal stresses can occur away from the input regions due to the term of lateral transmission of energy entering in the definition of the internal stress term. The term of lateral transmission of energy also redistributes the energy from regions of high input to regions where the wind energy input is small, such that the internal stresses act locally as a source of KE.

The degree of convergence of the numerical solver does not significantly affect the KE balance. We observe that the amount of (monthly mean Arctic averaged) energy dissipation/input by each term in the KE balance is stable after only a few Newton loop iterations in the nonlinear solver. This is in agreement with results previously shown by *Lemieux et al*. [2008] that only 10 Newton loops (NL) iterations are required for the average KE in the pack to stabilize to values that are within 2% of the KE of the fully converged solution. However, the degree of the convergence of the simulations could affect the deformation distributions in an analogous manner as with a change of spatial resolution. The particular effect of a changing deformation distribution on the amount of energy dissipated is yet to be evaluated.

Appendix A: Derivation of the Deformation Rate of Work in Terms of Stress and Strain Rates Invariants

In *Rothrock* [1975] and *Coon et al*. [1974], the deformation rate of work done by the internal stresses, $\mathrm{tr}\,(\dot{\epsilon} : \sigma)$, is written in terms of the stress and strain rate invariants. To derive this expression, we consider the following stress and strain rate tensors:

$$\sigma = \begin{pmatrix} \sigma_{11} & \sigma_{12} \\ \sigma_{21} & \sigma_{22} \end{pmatrix} \qquad \dot{\epsilon} = \begin{pmatrix} \dot{\epsilon}_{11} & \dot{\epsilon}_{12} \\ \dot{\epsilon}_{21} & \dot{\epsilon}_{22} \end{pmatrix},$$

where σ_{ij} are the vertically integrated internal stresses (equation (6)) and $\dot{\epsilon}_{ij}$ are the strain rates defined by $\dot{\epsilon}_{i,j} = \frac{1}{2}\left(\partial_i u_j + \partial_j u_i\right)$. Both tensors are symmetric. The principal values (or eigenvalues) of these tensors are found by solving the characteristic equations $|\sigma - \lambda I| = 0$ and $|\dot{\epsilon} - \lambda I| = 0$, respectively. They are given by

$$\begin{aligned} \sigma_1 &= \left(\frac{\sigma_{11}+\sigma_{22}}{2}\right) + \sqrt{\left(\frac{\sigma_{11}-\sigma_{22}}{2}\right)^2 + \sigma_{12}^2} \\ \sigma_2 &= \left(\frac{\sigma_{11}+\sigma_{22}}{2}\right) - \sqrt{\left(\frac{\sigma_{11}-\sigma_{22}}{2}\right)^2 + \sigma_{12}^2} \end{aligned} \tag{A1}$$

and,

$$\dot{\epsilon}_1 = \left(\frac{\dot{\epsilon}_{11}+\dot{\epsilon}_{22}}{2}\right) + \frac{1}{2}\sqrt{(\dot{\epsilon}_{11}+\dot{\epsilon}_{22})^2 - 4(\dot{\epsilon}_{11}\dot{\epsilon}_{22} - \dot{\epsilon}_{12}^2)}$$
$$\dot{\epsilon}_2 = \left(\frac{\dot{\epsilon}_{11}+\dot{\epsilon}_{22}}{2}\right) - \frac{1}{2}\sqrt{(\dot{\epsilon}_{11}+\dot{\epsilon}_{22})^2 - 4(\dot{\epsilon}_{11}\dot{\epsilon}_{22} - \dot{\epsilon}_{12}^2)}\ . \tag{A2}$$

In the above, $\sigma_1(\dot{\epsilon}_1)$ and $\sigma_2(\dot{\epsilon}_2)$ represent the maximum and minimum normal stress (strain rate), respectively. These eigenvalues can also be found by rotating the original tensors by an angle θ derived from the rotation matrices, P_σ and $P_{\dot{\epsilon}}$, formed with the eigenvectors that are associated with the eigenvalues, i.e.,

$$P_\sigma^T : \sigma : P_\sigma = \sigma' = \begin{pmatrix} \sigma_1 & 0 \\ 0 & \sigma_2 \end{pmatrix}$$
$$P_{\dot{\epsilon}}^T : \dot{\epsilon} : P_{\dot{\epsilon}} = \dot{\epsilon}' = \begin{pmatrix} \dot{\epsilon}_1 & 0 \\ 0 & \dot{\epsilon}_2 \end{pmatrix}.$$

The trace and determinant of second-order tensors (like σ and $\dot{\epsilon}$) are mathematical invariants under similarity transformations. From them, we can form two different invariants for each tensors which have a useful physical meaning, e.g.,

$$\sigma_I = \frac{\mathrm{tr}\,(\sigma)}{2} = \frac{\sigma_1+\sigma_2}{2}$$
$$\sigma_{II} = \sqrt{\left(\frac{\mathrm{tr}\,(\sigma)}{2}\right)^2 - \det\sigma} = \frac{\sigma_1-\sigma_2}{2}\ , \tag{A3}$$

and,

$$\dot{\epsilon}_I = \mathrm{tr}\,(\dot{\epsilon}) = \dot{\epsilon}_1+\dot{\epsilon}_2$$
$$\dot{\epsilon}_{II} = \sqrt{(\mathrm{tr}\,(\dot{\epsilon}))^2 - 4(\det\dot{\epsilon})} = \dot{\epsilon}_1-\dot{\epsilon}_2\ . \tag{A4}$$

The invariants σ_I and σ_{II} represent the average normal stress and maximal shear stress at a point, respectively, while $\dot{\epsilon}_I$ and $\dot{\epsilon}_{II}$ are the sea-ice divergence and the maximum shear strain at a point.

The trace of the product of the diagonalized strain rate and stress tensors, $\mathrm{tr}\,(\dot{\epsilon}' : \sigma')$, can be written in terms of the rotation matrices P_σ and $P_{\dot{\epsilon}}$ as

$$\begin{aligned} \mathrm{tr}\,(\dot{\epsilon}' : \sigma') &= \mathrm{tr}\,(P_{\dot{\epsilon}}^T : \dot{\epsilon} : P_{\dot{\epsilon}} : P_\sigma^T : \sigma : P_\sigma) \\ &= \mathrm{tr}\left[\begin{pmatrix} \dot{\epsilon}_1 & 0 \\ 0 & \dot{\epsilon}_2 \end{pmatrix} : \begin{pmatrix} \sigma_1 & 0 \\ 0 & \sigma_2 \end{pmatrix}\right] \\ &= \dot{\epsilon}_1\sigma_1 + \dot{\epsilon}_2\sigma_2\ . \end{aligned} \tag{A5}$$

Taking into account the fact that the rotation matrices are orthogonal (i.e., $P_i^T = P_i^{-1}, i = \dot{\epsilon}, \sigma$) and assuming that the principal axes of stress and strain rate coincide (i.e., $P_\sigma = P_{\dot{\epsilon}} = P$), the trace of the product of the diagonal tensors (A5) can be written as

$$\begin{aligned} \mathrm{tr}\,(\dot{\epsilon}' : \sigma') &= \mathrm{tr}\,(P^T : (\dot{\epsilon} : \sigma) : P) \\ &= \mathrm{tr}\,(P^{-1} : (\dot{\epsilon} : \sigma) : P) \\ &= \mathrm{tr}\,((\dot{\epsilon} : \sigma)') \\ &= \dot{\epsilon}_1\sigma_1 + \dot{\epsilon}_2\sigma_2, \end{aligned}$$

which can be interpreted as the trace of the rotated tensor $(\dot{\epsilon} : \sigma)$. Since the trace of a tensor is invariant under similarity transformations such as rotation, we can write

$$\mathrm{tr}\left((\dot{\epsilon} : \sigma)'\right) = \mathrm{tr}\left(\dot{\epsilon} : \sigma\right) = \dot{\epsilon}_1\sigma_1 + \dot{\epsilon}_2\sigma_2 \ .$$

Substituting the principal stresses and strain rates in terms of the invariants (equations (A3) and (A4)), we write [*Coon et al.*, 1974; *Rothrock*, 1975]:

$$\mathrm{tr}\left(\dot{\epsilon} : \sigma\right) = \dot{\epsilon}_I\sigma_I + \dot{\epsilon}_{II}\sigma_{II} \ . \tag{A6}$$

This term includes the rate of change of potential energy during deformations as well as the rates of dissipation from all energy sinks including frictional losses during ridging, shearing and viscous creep in the case of VP models.

Acknowledgments

Amélie Bouchat is grateful to the Natural Science and Engineering and Research Council (NSERC) and the Fonds Québécois de la Recherche sur la Nature et les Technologies (FQRNT) for scholarships received during the course of this work. Bruno Tremblay is grateful for financial support by the NSERC Discovery program, the Environment Canada Grants and Contribution program, and by the Office of Naval Research (N000141110977). This research was also supported by the Canadian Sea Ice and Snow Evolution (CanCISE) Network, which is funded by the NSERC's Climate Change and Atmospheric Research Program. We thank Jean-François Lemieux Jaime Palter and anonymous reviewers for their careful review of the manuscript and helpful comments.

References

Campbell, W. J. (1965), The wind-driven circulation of ice and water in a polar ocean, *J. Geophys. Res.*, *70*(14), 3279–3301.

Coon, M. D., and R. S. Pritchard (1979), Mechanical energy considerations in sea ice dynamics, *J. Glaciol.*, *24*(90), 377–389.

Coon, M. D., G. A. Maykut, R. S. Pritchard, D. A. Rothrock, and A. S. Thorndike (1974), Modeling the pack ice as an elastic-plastic material, *AIDJEX Bull.*, *24*, 1–105.

Dansereau, V. (2011), Are sea-ice model parameters independent of convergence and resolution?, MS thesis, McGill Univ., Montreal, Que.

Dempsey, J. P., R. M. Adamson, and S. V. Mulmule (1999), Scale effects on the in-situ tensile strength and fracture of ice. Part II: First-year sea ice at Resolute, N.W.T., *Int. J. Fract.*, *95*, 347–366.

Dumont, D., Y. Gratton, and T. E. Arbetter (2009), Modeling the dynamics of the North Water polynya ice bridge, *J. Phys. Oceanogr.*, *39*, 1448–1461, doi:10.1175/2008JPO3965.1.

Glen, J. W. (1970), Thoughts on a viscous model for sea ice, *AIDJEX Bull.*, *2*, 18–27.

Hibler, W. D. (1974), Differential sea-ice drift. II. Comparison of mesoscale strain measurements to linear drift theory predictions, *J. Glaciol.*, *13*(69), 457–471.

Hibler, W. D. (1977), A viscous sea ice law as a stochastic average of plasticity, *J. Geophys. Res.*, *82*(27), 3932–3938.

Hibler, W. D. (1979), A dynamic thermodynamic sea ice model, *J. Phys. Oceanogr.*, *9*, 815–946.

Hunke, E. C., and J. K. Dukowicz (1997), An elasticviscousplastic model for sea ice dynamics, *J. Phys. Oceanogr.*, *27*, 1849–1867.

Kundu, P. K., and I. M. Cohen (2008), *Fluid Mechanics*, 4th ed., chap. 4, pp. 81–137, Elsevier, Burlington, Mass.

Kwok, R. (2001), Deformation of the arctic ocean sea ice cover: November 1996 through April 1997, in *Scaling Laws in Ice Mechanics and Dynamics*, edited by J. Dempsey and H. H. Shen, pp. 315–323, Kluwer Acad, Dordrecht.

Lemieux, J.-F., and B. Tremblay (2009), Numerical convergence of viscous-plastic sea ice models, *J. Geophys. Res.*, *114*, C05009, doi:10.1029/2008JC005017.

Lemieux, J.-F., B. Tremblay, S. Thomas, J. Sedláček, and L. A. Mysak (2008), Using the preconditioned Generalized Minimum RESidual (GMRES) method to solve the sea-ice momentum equation, *J. Geophys. Res.*, *113*, C10004, doi:10.1029/2007JC004680.

Lemieux, J.-F., B. Tremblay, J. Sedláček, P. Tupper, S. Thomas, D. Huard, and J.-P. Auclair (2010), Improving the numerical convergence of viscous-plastic sea ice models with the Jacobian-free Newton-Krylov method, *J. Comput. Phys.*, *229*, 2840–2852, doi:10.1016/j.jcp.2009.12.011.

McPhee, M. G. (1975), Ice-ocean momentum transfer for the AIDJEX ice model, *AIDJEX Bull.*, *29*, 93–111.

Miller, P. A., S. W. Laxon, and D. L. Feltham (2005), Improving the spatial distribution of modeled Arctic sea ice thickness, *Geophys. Res. Lett.*, *32*, L18503, doi:10.1029/2005GL023622.

Parmerter, R. R., and M. D. Coon (1973), Mechanical models of ridging in the Arctic sea ice cover, *AIDJEX Bull.*, *19*, 59–112.

Pritchard, R. S. (1981), Mechanical behavior of pack ice, in *Mechanical Behavior of Structured Media*, edited by A. P. S. Selvadurai, pp. 371–405, Elsevier, Amsterdam.

Pritchard, R. S. (2001), Long-term sea ice dynamics simulations using an elastic-plastic constitutive law, *J. Geophys. Res.*, *106*(C12), 31,333–31,343, doi:10.1029/2000JC000638.

Pritchard, R. S. (2005), Stability of sea ice dynamics models: Viscous-plastic rheology, replacement closure, and tensile cutoff, *J. Geophys. Res.*, *110*, C12010, doi:10.1029/2003JC001875.

Richter-Menge, J. A. (1997), Towards improving the physical basis for ice-dynamics models, *Ann. Glaciol.*, *25*, 177–182.

Rothrock, D. A. (1975), The energetics of the plastic deformation of pack ice by ridging, *J. Geophys. Res.*, *80*(33), 4514–4519.

Smith, D. R. (1993), An introduction to continuum mechanics—After Truesdell and Noll, in *Solid Mechanics and Its Applications*, vol. *22*, 253–268 pp., Springer, Netherlands.

Steele, M., J. Zhang, D. Rothrock, and H. Stern (1997), The force balance of sea ice in a numerical model of the Arctic Ocean, *J. Geophys. Res.*, *102*(C9), 21,061–21,079.

Steele, M., R. Morley, and W. Ermold (2001), PHC: A global ocean hydrography with a high-quality arctic ocean, *J. Clim.*, *14*, 2079–2087.

Stern, H. L., D. A. Rothrock, and R. Kwok (1995), Open water production in Arctic sea ice: Satellite measurements and model parametrizations, *J. Geophys. Res.*, *100*(C10), 20,601–20,612.

Thorndike, A. S., D. A. Rothrock, G. A. Maykut, and R. Colony (1975), The thickness distribution of sea ice, *J. Geophys. Res.*, *80*(33), 4501–4513.

Tremblay, B., and L. A. Mysak (1997), Modeling sea ice as a granular material, including the dilatancy effect, *J. Phys. Oceanogr.*, *27*, 2342–2360.

Wang, K., and C. Wang (2009), Modeling linear kinematic features in pack ice, *J. Geophys. Res.*, *114*, C12011, doi:10.1029/2008JC005217.

Zhang, J., and W. Hibler (1997), On an efficient numerical method for modeling sea ice dynamics, *J. Geophys. Res.*, *102*(C4), 8691–8702.

Zhang, J., and D. Rothrock (2000), Modeling Arctic sea ice with an efficient plastic solution, *J. Geophys. Res.*, *105*(C2), 3325–3338.